

Università degli Studi di Padova



Dipartimento di Fisica e Astronomia “Galileo Galilei”

Corso di Laurea in Fisica

Tesi Triennale

**CHARACTERIZATION WITH DIGITAL
ELECTRONICS OF A NEUTRON DETECTOR FOR
FAST NEUTRONS**

Candidato: **Andrea Raggio**

Matricola: **1069502**

Relatori: **Dott. G. Jaworski**
Dott. V. Modamio
Dott. J.J. Valiente-Dobón
Prof. D. Mengoni

Anno accademico 2016-2017

Contents

Introduction	1
1 Scintillation Detectors	3
1.1 Organic scintillators	3
1.2 Fast Neutron Detection	5
2 Digital Data Analysis	9
2.1 Timing	12
2.1.1 Digital Constant Fraction Discrimination	12
2.2 Pulse Shape Analysis	13
2.2.1 Charge Comparison	15
2.2.2 Integrated Rise Time	17
3 NEDA Characterization Measurements	19
3.1 The Detector	19
3.2 Timing Measurement	21
3.2.1 CFD Parameters Optimization	23
3.2.2 Results	24
3.3 Neutron- γ Discrimination Measurement	27
3.3.1 Analog NGD	28
3.3.2 Digital NGD	29
Summary and Conclusions	33
Bibliography	36

Introduction

Large neutron-detector arrays, such as the Neutron Wall [1, 2] and the Neutron Shell [3], were developed and successfully used in conjunction with γ -ray detectors to study the structure of neutron-deficient nuclei, producing excellent results during their physics campaigns. Nevertheless, the development of digital data analysis and the increase in efficiency of large HPGe γ -ray arrays demand new neutron detectors in order to pair their current performance. The *NEutron Detector Array* NEDA is the result of this need.

The NEDA project started in 2007 as an international collaboration of eight countries with the aim to build a new detector array to be used in conjunction with γ -ray detectors such as AGATA, GALILEO, EXOGAM2 and PARIS and to work with state-of-the-art digital electronics. Considerable effort has been put to develop an efficient device by performing simulations and measurements to optimize the detector design [4], and, finally in 2016, the definitive production of NEDA detectors started. The first physic campaign that will use NEDA is scheduled in 2018 at GANIL, France, where NEDA will be coupled to the γ -tracking array AGATA [5].

Within this thesis, an introduction to detection techniques, digital analysis algorithms and the characterization of a single NEDA detector in terms of timing [6] and pulse shape discrimination [7] will be discussed.

Chapter 1

Scintillation Detectors

The use of scintillation light produced by certain materials is one of the first techniques used to detect a wide variety of radiation and it is still considered one of the most suitable methods to detect fast neutrons. The choice of a scintillator material is done taking into account several factors:

- the scintillation efficiency: what fraction of the incoming radiation is converted into detectable light;
- the linearity of this conversion as a function of the incoming particle energy;
- the decay time of the induced luminescence, which influences the time resolution of the generated pulse;
- the transparency of the material to the wavelength of its own emission;
- the capability to distinguish different kind of radiation;
- the cost and the difficulty in production of the material itself.

Two main families of materials exist nowadays: the inorganic and organic scintillators. The former are usually better in terms of efficiency and linearity, moreover the high Z -value and density of their constituents make them more suitable for γ -ray spectroscopy. The latter, instead, are hydrogen-based and therefore much more efficient for fast neutron detection and *Neutron Gamma Discrimination* (NGD). NEDA uses an organic scintillator for neutron detection, thus, in the next section, a description of the working principles behind this kind of detector will be given.

1.1 Organic scintillators

Three kind of processes rule the emission of scintillation light by an organic scintillator: the *fluorescence* is the quick production of radiation after the excitation of a substance, the *phosphorescence*, instead, is the emission of longer wavelength radiation than fluorescence with a slower characteristic time. Finally the *delayed*

fluorescence consists in the same kind of radiation as the fluorescence, but with a greater emission time. An important characteristic of organics is the production of fluorescence light from transitions in the energy structure of a single molecule, allowing the process to be independent from the physical state of the compound. This enables the development of different kinds of organic scintillators, such as polycrystalline, gaseous, or liquid organic detectors. The electronic transitions of the organic molecules, which are the basis of the scintillation process, can be explained taking in consideration the π -electron structure (see Fig 1.1). The singlet (spin=0) and triplet (spin=1) states are labelled respectively S_0, S_1, S_2, S_3 and T_1, T_2, T_3 .

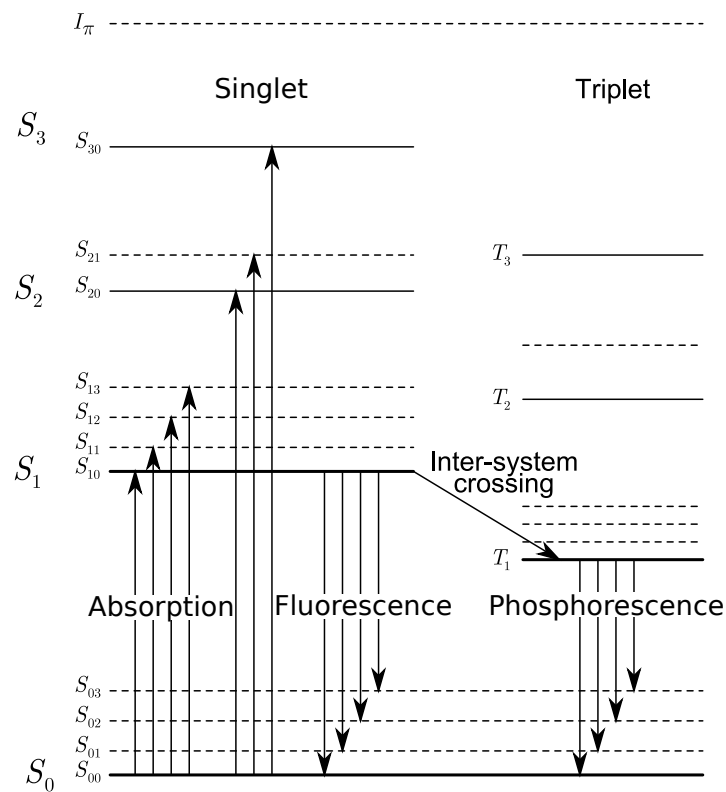


Figure 1.1: π -electronic energy level of an organic molecule

Moreover, each of these electronic configurations is further subdivided into finer levels, which represent vibrational states of the molecule. For the scintillation materials, usually, the singlet energy separation between S_1 and S_0 is 3 or 4 eV, while the gap among the vibrational states is of the order of 0.15 eV. Consequently, at room temperature, the average thermal energy (0.025 eV) is lower than the first vibrational states, and nearly all the molecules are in the S_0 state.

When a charged particle interacts with the medium, part of its kinetic energy is absorbed and the scintillation molecules change their energy states. Then,

through non-radiative internal conversions, the higher singlet energy states are quickly (some picoseconds) de-excited to S_1 levels. The fluorescence light is emitted in transitions between this state and one of the ground vibrational states. For an organic scintillator the typical decay time of this kind of transitions is of the order of nanosecond. A singlet S_1 state may also be converted into a triplet T_1 state, through a so called intersystem crossing. The phosphorescence light is generated by transitions between T_1 and S_0 states with characteristic decay time that could be as much as 10^{-3} seconds. Moreover, the T_1 - S_0 energy gap is smaller than for S_1 - S_0 transitions, explaining the longer wavelength of the phosphorescence light. Finally, the delayed fluorescence light, is produced when a molecule in T_1 state is thermally excited back to the S_1 state. The different energy gap between the excitation and de-excitation transitions explain also the transparency of the material to its own emitted light. Anyway, usually a component that behaves as a "wavelength shifter" is added to the mixture in order to match closer the spectral sensitivity of the photomultiplier.

Commonly, in an organic scintillator, the prompt fluorescence is the uppermost light emission, however, a delayed fluorescence component is also observed in many cases. Their composition produces a signal that could be represented by two exponential decays, called the fast and the slow component. Especially in neutron detection, the latter, yield very useful information. Indeed, the quantity of delayed fluorescence light depends on the nature of the interacting particle. Slow component originates primarily from the excitation of triplet states along the track of ionization, a bimolecular interaction between two such excited molecules leads to a change of their electronic states, producing one in the singlet S_1 state, which is responsible of the delayed fluorescence, and the other one in the ground state. The rate of this kind of reaction depends on the square of the triplet density along the ionization path, therefore it is sensitive to the rate of energy loss dE/dx of the interacting particle. The analysis of the slow component contribution to the signal thus allows to differentiate among interactions of particles of different kind, this process is called *Pulse Shape Discrimination* (PSD). This PSD capacity makes organic scintillators the best choice for fast neutron detection. Moreover, organics, have an high cross section for fast neutrons to scatter with protons and produce fast signals, resulting in large efficiency in neutron detection and high timing performance.

1.2 Fast Neutron Detection

The detection process of neutral particles, such as neutrons, involves the elastic scattering of the particles on light nuclei. The kinetic energy is transferred to a recoil charged particle (either an e^- or a light nuclei as protons or alphas). Thus, neutron detector based on this interaction are called *proton recoil detectors*.

Fig. 1.2 shows a scheme of an elastic scattering in center of mass and laboratory systems.

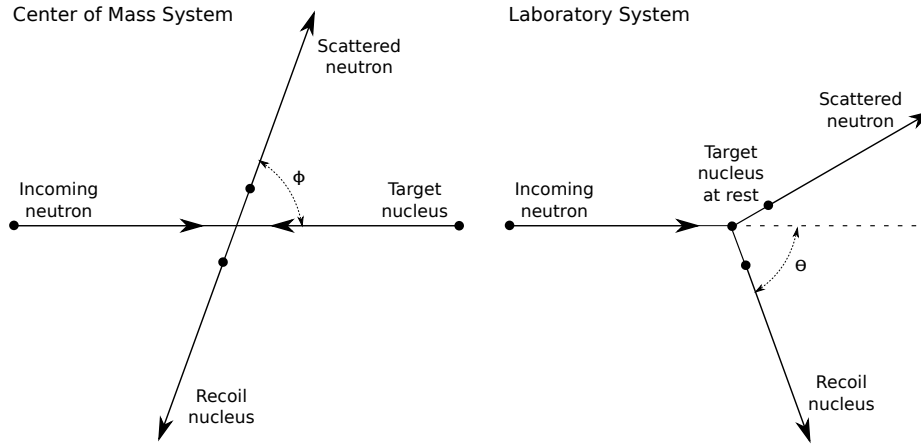


Figure 1.2: Elastic scattering of a neutron with a target nucleus at rest in the laboratory and center of mass systems

If A is the target mass and E_n the incoming neutron kinetic energy in the laboratory system, E_R , the recoil nucleus kinetic energy, is given by :

$$E_R = \frac{2A}{(1+A)^2} (1 - \cos \Phi) E_n \quad (1.1)$$

which in terms of the laboratory scattering angle θ of the recoil nucleus becomes:

$$E_R = \frac{4A}{(1+A)^2} (\cos^2 \theta) E_n \quad (1.2)$$

Eq 1.2 predicts the energy range of the recoil nucleus. If the scattering angle tends to be perpendicular, the energy tends to zero, for a null scattering angle, instead, the utmost value is reached and depends on the target nucleus mass:

$$E_R|_{max} = \frac{4A}{(1+A)^2} E_n \quad (1.3)$$

Tab. 1.1 lists the maximum fraction of kinetic energy transferred by the elastic scattering for different target nuclei. The greater is the target mass the less is the fraction of transferred energy. Only 1_1H allows to fully transfer the incoming neutron energy, and for this reason light nuclei are preferred in fast neutrons detection.

The recoil energy distribution function is given by:

$$P(E_R) = \frac{(1+A)^2}{A} \frac{\sigma(\Phi)}{\sigma_s} \frac{\pi}{E_n} \quad (1.4)$$

with $\sigma(\Phi)$ the differential scattering cross section and σ_s the total scattering cross section integrated over all angles. Eq. 1.4 shows that the energy distribution follows the shape of $\sigma(\Phi)$, then if the cross section does not depend on Φ , i.e. the scattering

Table 1.1: Maximum energy transfer in neutron elastic scattering with target nucleus at rest in laboratory system

Target Nucleus	A	$\frac{E_R}{E_n} \Big _{max}$
1_1H	1	1
2_1H	2	0.889
3_2He	3	0.750
4_2He	4	0.640
${}^{12}_6C$	12	0.284
${}^{16}_8O$	16	0.221

process is isotropic in the center of mass system, a simplification is possible. This circumstance happens with scattering from Hydrogen, in the range of interest ($E_n < 10$ MeV). In this case the energy distribution is flat from zero to the full incident neutron energy, and therefore the average recoil energy is $1/2 E_n$.

The efficiency of a proton recoil detector composed of a single specie is evaluated as:

$$\varepsilon = 1 - \exp(-N\sigma_s d) \quad (1.5)$$

where N is the density of target, σ_s its scattering cross section and d the neutrons path length through the detector. However, Carbon often appears in scintillation detectors in combination with Hydrogen, consequently Eq. 1.5 becomes:

$$\varepsilon = \frac{N_H \sigma_H}{N_H \sigma_H + N_C \sigma_C} \{1 - \exp[-(N_H \sigma_H + N_C \sigma_C) d]\} \quad (1.6)$$

NEDA detector uses EJ-301 (BC501 A) as a liquid scintillator. It is well known for its excellent pulse shape discrimination properties. Its characteristics are listed in Tab. 1.2.

Table 1.2: The proprieties of EJ-301 liquid scintillator

Light Output (% Anthracene)	78
Scintillation Efficiency (photons/1 MeV e ⁻)	12000
Wavelength of Maximum Emission (nm)	425
Decay Time, Short Component (ns)	3.2
Mean Decay Times of First 3 Componenets (ns)	3.16, 32.3, 270
Bulk Light Attenuation Length (m)	2.5-3
Specific Gravity	0.874
Refractive Index	1.505
Flash Point (°C)	26
Boiling Point (°C at 1 atm)	141
No. of H atoms per cm ³ (10 ²²)	4.82
No. of C atoms per cm ³ (10 ²²)	3.98
No. of Electrons per cm ³ (10 ²³)	2.27

Chapter 2

Digital Data Analysis

NEDA will make use of digital electronics based on NUMEXO2 cards [8, 9] and state-of-the-art digital signal processing. In the following pages a description of digital electronics and algorithms used to characterize the detector is given.

Digital signal processing is spreading in nuclear physics and is replacing the analog one. This is due to several reasons:

- one single board can do energy, timing and pulse shape analysis reducing drastically the costs;
- digital techniques allow better correction of the baseline fluctuation effects;
- it is possible to keep synchronized and correlated several channels and make coincidence/anticoincidence after the acquisition (off-line);
- it is possible to change and adapt the online working algorithm tailoring it to the application;
- it is possible to perform a more accurate signal treatment.

The simplified scheme of the experimental set-up used, employing digital electronics, in the measurements described in this thesis is shown in Fig. 2.1.

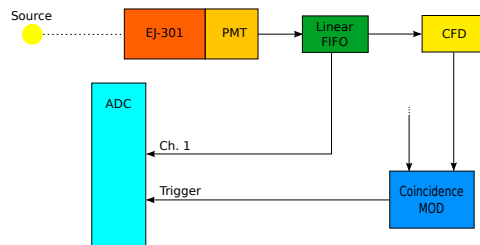


Figure 2.1: Simplified representation of experimental set-up with a flash *Analog to Digital Converter* (ADC) device.

The heart of the digitalization process is the *Analog to Digital Converter (ADC)*, which transforms, as the name suggests, the analog signals from the detector into the digital ones. In Fig. 2.1 the anode signal from the detector is split thanks to a linear *Fan-in Fan-out (FIFO)*, in order to send one output directly to the ADC, and the other one to an analog *Constant Fraction Discriminator (CFD)* module, linked to a coincidence unit to produce the trigger signal for the digitizer. The complete experimental set-up used in the measurements to characterize NEDA is described in Ch. 3.

Important parameters for ADCs used in detection systems are:

- sampling frequency;
- dynamic range;
- bit-resolution;
- differential non-linearity;
- integral non-linearity;
- count-rate performance.

The simplest technique is flash conversion (see Fig. 2.2). A signal is fed in parallel

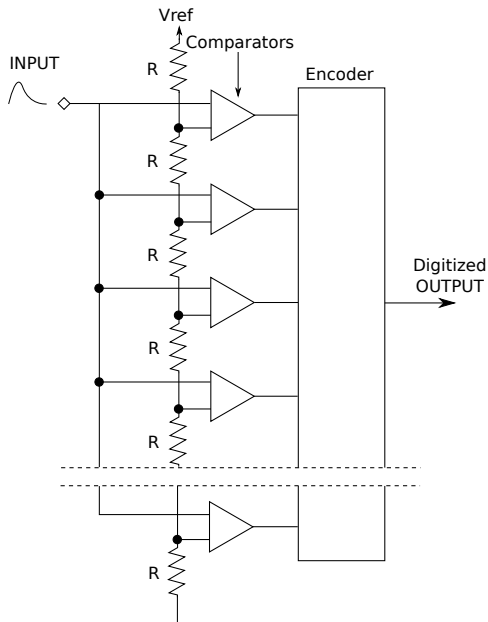


Figure 2.2: Block diagram of a flash ADC, showing the threshold comparators fed by resistive divider.

to a bank of threshold comparators, and the individual threshold levels are set by a resistive divider. The comparators outputs are encoded such that the output of the highest level comparator that fires, yields the correct bit pattern. The main advantage of this method is speed, conversion times smaller than 10 ns are readily achievable; the drawbacks are components count and power consumption, as one comparator is needed for every conversion bin. In the final experimental set-up, the anode waveforms produced by the detector were digitized by a sampling ADC of model Struck SIS3350. At the same time, in order to allow a comparison between the analog and digital results, the former processed signals were digitized with a Struck SIS3302. In Tab. 2.1 the features lists of the two ADCs are reported.

Table 2.1: Lists of features of the two ADC devices, Struck SIS3350 and SIS3302, used in the experiment.

SIS3350	SIS3302
Single width 6U VME card	Single width 6U VME card
4 channels	8 channels
500 MS/s	100 MS/s
128 MSamples/channel memory	32 MSamples/channel memory
250 MHz bandwidth	50 MHz bandwidth
Internal/External clock	Internal/External clock
Readout in parallel to acquisition	Readout in parallel to acquisition
Pre/Post trigger capability	Pre/Post trigger capability
Trigger OR output (4 individual thr.)	Trigger OR output (8 individual thr.)
1/2/4 GBit/s optical link option	1-wire Id. serial PROM

In Fig. 2.3 the average digitized NEDA waveform produced by a ^{60}Co γ -source is shown, obtained from 10 thousand signals normalized over total charge and baseline subtracted. The digitalization process is represented by the red sampling points separated by 2 ns, as an effect of the ADC sampling frequency of 500 MHz. An spline interpolation algorithm is then necessary to reconstruct the pulse.

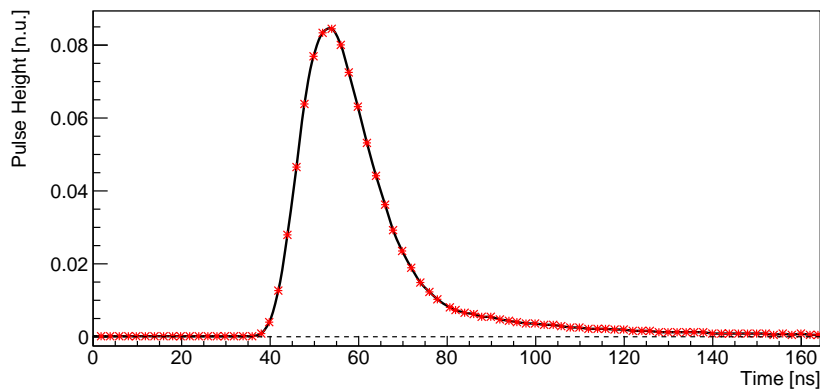


Figure 2.3: NEDA waveform produced by a ^{60}Co γ -source, obtained from ten thousand signals normalized over total charge and baseline subtracted. In red the sampling points of the ADC.

To characterize the NEDA detector in terms of timing and neutron- γ discrimination performances the choice and tuning of the analysis algorithms are decisive. In the two following sections the chosen algorithms are described.

2.1 Timing

In particle detection one of the first and most important requirements is the production of a time reference for detected events. Correct definition of the time of a particle detection is essential to allow the production of coincidence signals between the different detectors which compose the arrays of an experimental set-up. Moreover the reduction of the timing error of the system is crucial for several measurements, such as the *Time of Flight* (TOF) technique, used to distinguish the particle type but also to measure its kinetic energy.

There are several ways to produce a timing reference for detected particles, the aim of a good technique is to increase the accuracy and reduce the dependence on particle energy (*Time walk*). The simplest one is the *Leading Edge* method, which associates the time reference of the signal with the crossing moment of a fixed threshold, for instance 0.2 as shown in Fig. 2.4-a. In scintillation detectors, where the rising time of the pulses is constant, this method is clearly affected by the amplitude of the signals, making it not good for the purpose. A better solution is the *Constant Fraction Discrimination* (CFD) technique (Fig. 2.4-b), which gives a time reference independent on pulse amplitude.

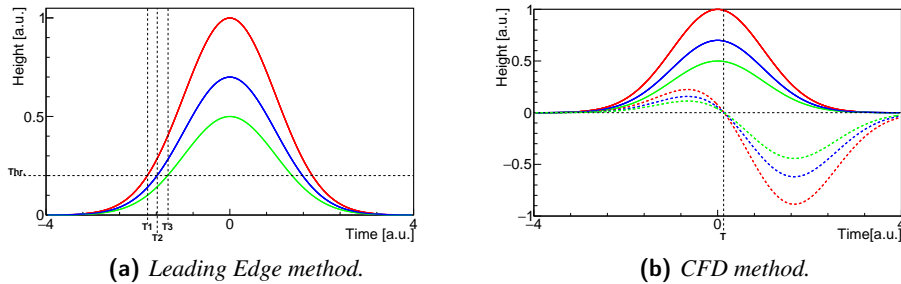


Figure 2.4: *Leading Edge* (a) and *Constant Fraction Discrimination* (CFD) (b) techniques applied on three Gaussian pulses with same mean and sigma but different amplitudes. The bipolar dashed pulses in b) are generated by the CFD algorithm.

2.1.1 Digital Constant Fraction Discrimination

The CFD method works generating a bipolar signal from the original pulse and then finding its zero crossing as time reference. Lets name W_t the digitized waveform with t an integer number (sample number). The bipolar pulse P_t is calculated as:

$$P_t = \chi W_t - W_{t-\delta}, \quad (2.1)$$

where χ is a reduction fraction and δ an integer delay. Fig. 2.5 shows the CFD method applied on a NEDA signal.

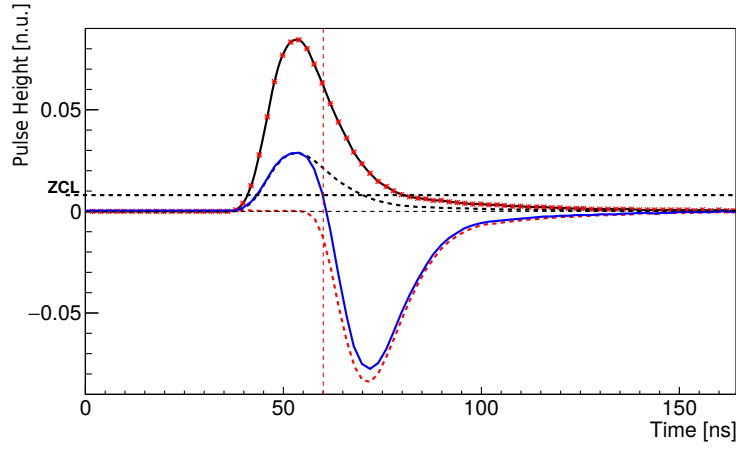


Figure 2.5: CFD algorithm applied on a NEDA pulse produced by a ^{60}Co γ -source, obtained from 10 thousand signals normalized over total charge and baseline subtracted. In black the original pulse, in dashed black and dashed red the reduced and the delayed one, in blue the bipolar signal.

After choosing a *zero crossing line* (ZCL) in order to minimize the time walk, is possible to obtain the intersection with the bipolar signal by taking the samples above and below ZCL value and interpolating to find the time reference. A cubic spline interpolation with derivative bound continuity condition up to second order was chosen. Lets consider the sample range $[t_{-1}, t_0]$ with t_0 the first sampled point after the intersection and t_{-1} the preceding one. The reconstructed pulse $f(t)$ inside the range is evaluated as follow:

$$\mathbf{f}(\mathbf{t}) = \mathbf{a}(\mathbf{t} - \mathbf{t}_{-1})^3 + \mathbf{b}(\mathbf{t} - \mathbf{t}_{-1})^2 + \mathbf{c}(\mathbf{t} - \mathbf{t}_{-1}) + \mathbf{d}$$

$$\begin{cases} a = 1/18(P_{t_{-3}} - 8P_{t_{-2}} + 19P_{t_{-1}} - 19P_{t_0} + 8P_{t_1} - P_{t_2}) \\ b = 1/30(-4P_{t_{-3}} + 32P_{t_{-2}} - 58P_{t_{-1}} + 37P_{t_0} - 8P_{t_1} + P_{t_2}) \\ c = 1/90(7P_{t_{-3}} - 56P_{t_{-2}} - 11P_{t_{-1}} + 74P_{t_0} - 16P_{t_1} + 2P_{t_2}) \\ d = P_{t_{-1}} \end{cases}$$

2.2 Pulse Shape Analysis

The ratio between prompt and delayed fluorescence in organic scintillators is a key factor for neutron detectors. TOF neutron discrimination technique, for instance, needs two detectors in coincidence to work. Thanks to the different speed of neutrons and γ rays it is possible to distinguish them. Instead, a method which evaluates the prompt to delayed fluorescence ratio is able to discriminate particle type using only the information carried by the signal produced from a single detector.

In Fig. 2.6 a clear difference is visible between a γ -ray and a neutron signals: the greater presence of delayed fluorescence in neutrons waveforms results in a longer tail with respect to γ rays.

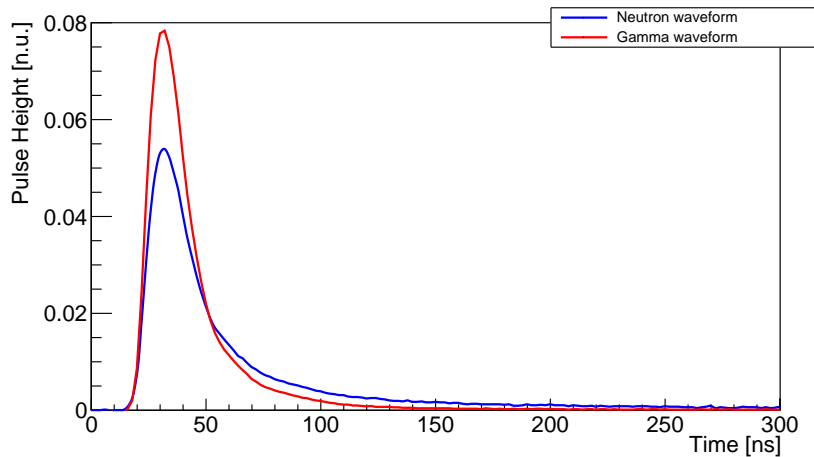


Figure 2.6: Neutrons and γ -rays waveforms from NEDA produced by a ^{252}Cf source, obtained from one thousand signals normalized over total charge and baseline subtracted. The digital TOF spectrum was used for the selection of the interacting particle type.

The total neutron detection capability of a detector is the combination of the neutron detection and the identification efficiencies. Due to the neutral charge of neutrons, as mentioned in Sec. 1.2, the detection process involves an elastic scattering with light nuclei, transferring a large part of the neutrons kinetic energy. The different prompt to delayed fluorescence ratio with respect to γ rays is due to this first interaction inside the scintillator. For this reason PSA algorithms have a greater efficiency for smaller volume detectors. Moreover, larger volumes are essential for a high particles detection efficiency. Consequently, a compromise between the two characteristics is necessary. In the following pages, two digital methods used in the characterization of the detector, which are based on the different ratio between fast and slow components of the signal of neutrons and γ rays, will be described.

2.2.1 Charge Comparison

The *Charge Comparison* (CC) method is based on the choice of two integration gates on the digitized pulse $W(t)$: a short one, sensitive to the particle nature, and a long one, accounting for the total charge, to normalize with (see Fig. 2.7).

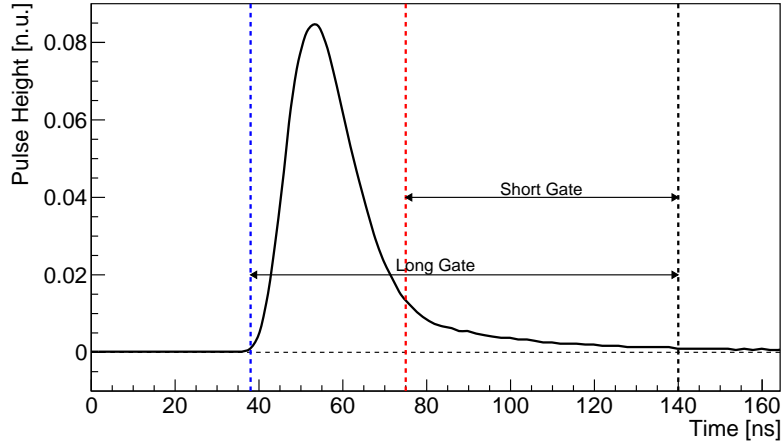


Figure 2.7: Charge Comparison integration gates for a NEDA digitized signal.

In the code used for the neutron- γ discrimination characterization three parameters were selected: the start integration time t_I , as number of samples before the CFD time reference t_C performed by the CFD algorithm, and the short t_S and long t_L integration times, defined as number of samples after t_C . A CC value, linked to the components ratio, is then obtained as:

$$CC = \frac{\int_{t_C+t_S}^{t_C+t_L} W(t) dt}{\int_{t_C-t_I}^{t_C+t_L} W(t) dt} \quad (2.2)$$

The CC distribution (see Fig. 2.8) shows two peaks corresponding to the two particle types. Neutrons shows a greater CC value than γ ray, due to a larger emission of delayed fluorescence light and consequently a longer tail.

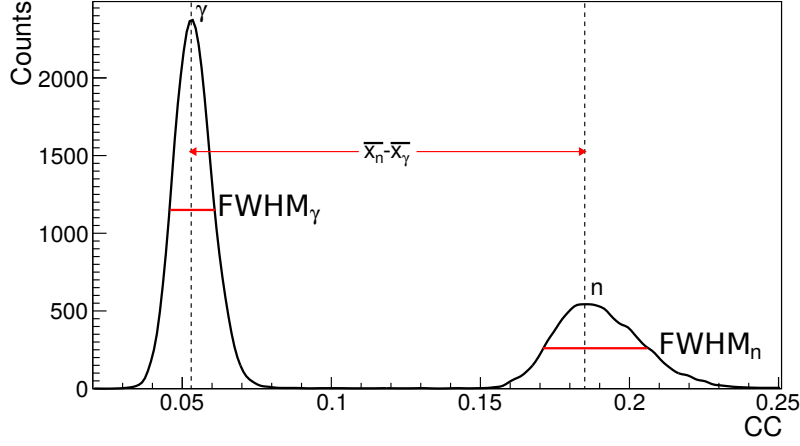


Figure 2.8: CC value distribution with neutrons and γ rays produced by a ^{252}Cf source, selecting events with energy between 600 keVee and 800 keVee. The two FWHM values and the difference between the centroids are represented in red.

Then, to evaluate the detector performance, the *Figure of Merit* (FOM) is calculated as the ratio between the distance of the peaks centroids ($\bar{x}_n, \bar{x}_\gamma$) and the sum of the two FWHM values:

$$\text{FOM} = \frac{|\bar{x}_n - \bar{x}_\gamma|}{\text{FWHM}_n + \text{FWHM}_\gamma} \quad (2.3)$$

To correctly evaluate the parameters of the two peaks a fit was necessary. Two fitting functions composed by a Gaussian peak with two exponential tails [10] were used for the two peaks of the distribution:

$$f(x, \bar{x}, \sigma, k_L, k_R) = \begin{cases} e^{\frac{k_L^2}{2} + k_L \left(\frac{x-\bar{x}}{\sigma}\right)}, & \text{for } \frac{x-\bar{x}}{\sigma} \leq -k_L, \\ e^{-\frac{1}{2} \left(\frac{x-\bar{x}}{\sigma}\right)^2}, & \text{for } -k_L < \frac{x-\bar{x}}{\sigma} \leq k_R, \\ e^{\frac{k_R^2}{2} + k_R \left(\frac{x-\bar{x}}{\sigma}\right)}, & \text{for } k_R < \frac{x-\bar{x}}{\sigma}. \end{cases} \quad (2.4)$$

The FWHM was then calculated as a difference between the two edge points HWHM1 and HWHM2, estimated from the fit parameters:

$$\text{HWHM1} = \begin{cases} \bar{x} - \sigma \left(\frac{k_L}{2} - \frac{\ln(\frac{1}{2})}{k_L} \right), & \text{for } k_L < \ln(2)\sqrt{2}, \\ \bar{x} - \sigma \ln(2)\sqrt{2}, & \text{for } k_L \geq \ln(2)\sqrt{2}. \end{cases} \quad (2.5)$$

$$\text{HWHM2} = \begin{cases} \bar{x} + \sigma \left(\frac{k_R}{2} - \frac{\ln(\frac{1}{2})}{k_R} \right), & \text{for } k_R > \ln(2)\sqrt{2}, \\ \bar{x} + \sigma \ln(2)\sqrt{2}, & \text{for } k_R \leq \ln(2)\sqrt{2}. \end{cases} \quad (2.6)$$

The CC integration gates were optimized in order to reach the best FOM value.

2.2.2 Integrated Rise Time

The *Integrated Rise Time* (IRT) technique is based on the rising time of the *Cumulative Integration* (CI) function of the digitized signal, defined as:

$$CI(t) = \int_0^t W(s) ds \quad (2.7)$$

The time difference between the moment the CI function reaches a fixed fraction (α) of the total charge integral and the digital CFD reference is picked as an IRT indicator (see Fig. 2.9). The total charge integral is evaluated as an average of the last one hundred samples of the CI function, in order to reduce possible errors from baseline fluctuation effects.

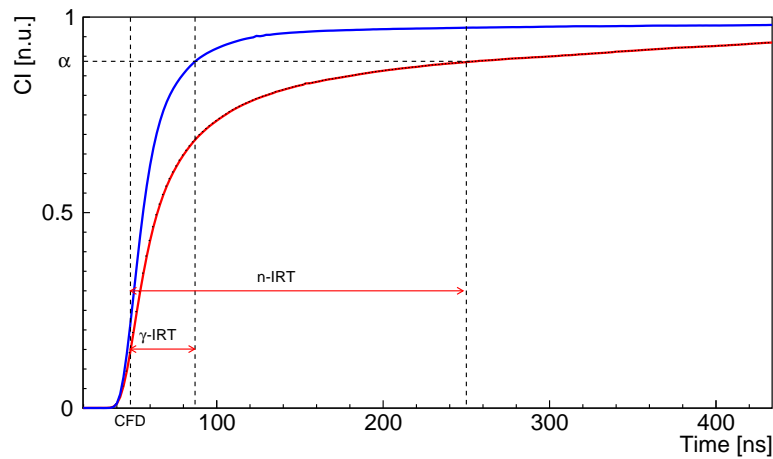


Figure 2.9: Cumulative integration functions for neutron (red) and γ ray (blue). The functions were obtained from the average digitized pulses of neutrons and γ rays produced by a ^{252}Cf source and selected by the digital TOF spectrum. The rise time, evaluated as difference between the time when CI function reaches the α fraction of the total charge integral and the CFD reference, is also shown.

Similarly to the CC method, the IRT value is greater for neutrons, having a larger slow component with respect to γ rays, and consequently obtaining the same kind of distribution of the CC technique (see Fig. 2.10). Again the performance of the detector is evaluated performing a fit of the IRT distribution and calculating the FOM value.

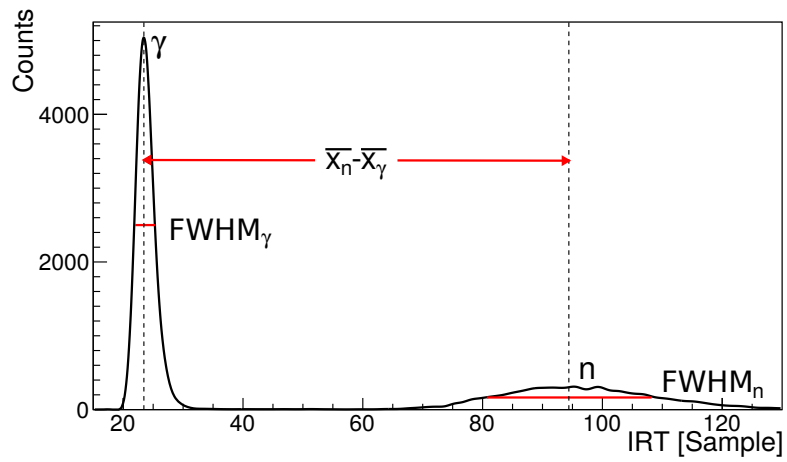


Figure 2.10: IRT value distribution with neutrons and γ rays produced by a ^{252}Cf source, selecting events with energy between 600 keVee and 800 keVee. The two FWHM values and the difference between the centroids are represented in red.

Chapter 3

NEDA Characterization Measurements

3.1 The Detector

NEDA detector is made with an organic liquid scintillator (see Sec. 1.1). It consists of two matching bodies, a scintillation chamber and a *Photo Multiplier Tube* (PMT) housing (see Fig. 3.1), both sharing the same hexagonal profile with 146 mm side to side distance.

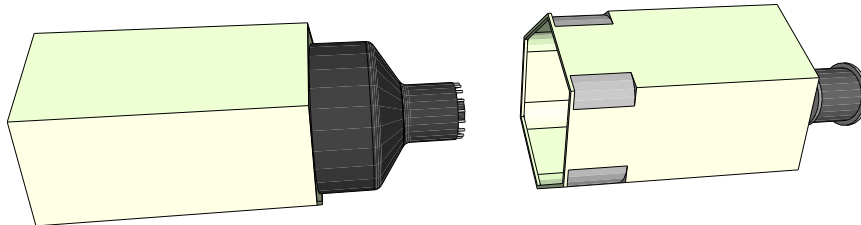


Figure 3.1: NEDA detector design, the scintillation chamber the *Photo Multiplier Tube* (PMT) and his housing are visible.

The scintillation chamber has an active volume of ~ 3.15 l and a total length of 205 mm, with the inner surface coated with TiO_2 based reflective paint EJ-520. The top flange finishes with a 5" N-BK7 5 mm thick glass window, that reaches 92% transmittance for the wavelength of interest. A pipe connects the active volume of the detector with a bellow chamber, for thermal expansion, placed behind the PMT housing. The liquid organic scintillator EJ-301 (BC501 A) fills the detector scintillation chamber after being bubbled with a N_2 flux in order to eliminate the oxygen traces. Readout consist in a 5" diameter and optically coupled to the glass window photomultiplier, fitted inside a 1 mm thick cylinder of μ -metal serving as a magnetic shielding and, as mentioned, housed in the hexagonal case. This phototube, a model Hamamatsu R11833-100HA (see Tab. 3.1) with 35% *Quantum*

Efficiency (QE), fast rising time, 10-step dynodes and a transistorized *Voltage Divider* (VD), was chosen for its optimal performances for timing [11] and neutron- γ discrimination [12] purposes.

Table 3.1: Lists of features of the Hamamatsu R11833-100HA PMT.

Spectral Response [nm]	300/650
Wavelength of maximum response [nm]	420
Photocathode material	Bialkali
Photocathode minium effective area [mm diameter]	111
Window	Borosilicate glass
Direct interelectrode capacitance (Anode to last dynode) [pF]	6
Direct interelectrode capacitance (Anode to all other electrodes) [pF]	7
Operating ambient temperature [°C]	-30/50
Cathode quantum efficiency at 350 nm [%]	35
Gain	5.010^5
Anode pulse rise time [ns]	4
Electron transit time [ns]	45
Transit time spread (FWHM) [ns]	5.5

The main idea behind the NEDA project is to design and build an array with the highest possible neutron detection efficiency, excellent discrimination between neutrons and γ rays, and a small neutron scattering probability among detectors, for this reasons the possible array configurations were extensively studied [5, 13]. One important goal, in particular, was to increase the 2n efficiency (efficiency to detect events with two neutrons emitted) by a factor up to 5–10, compared to existing neutron detector arrays, like the mentioned Neutron Wall. Various geometries were studied, being the so called Staircase 2π (see Fig 3.2) the most efficient. It presents a 1n efficiency of 30.18%, and 4.99% for the 2n one, reaching the expected gain. This configuration uses 300 detectors, with a total scintillation volume of 945 l.

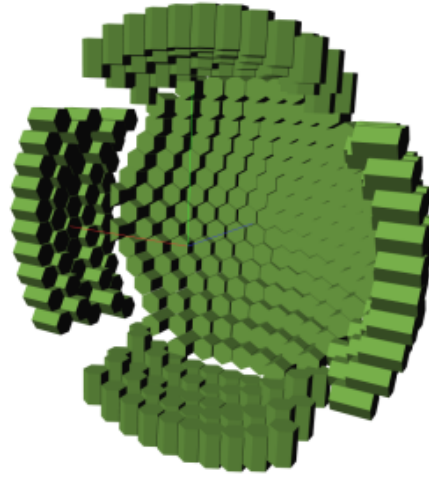


Figure 3.2: NEDA Staircase 2π configuration

3.2 Timing Measurement

In the following pages, the description of the characterization measurements performed on a NEDA detector will be discussed. Two experimental configurations were used to study timing and *Neutron γ Discrimination* (NGD) performances. Each one was designed to produce the digitized signals from the detector and in parallel to use analog electronics, in order to have a comparison between the two techniques.

To correctly characterize a NEDA detector on timing performance, an accurate time reference was necessary. For this reason a commercial 1" \times 1" BaF₂ scintillator detector was chosen. BaF₂ is presently the fastest known scintillator, able to reach time resolution up to 200 ps. Its characteristics are listed in Tab. 3.2.

A ⁶⁰Co γ -ray source was used for the measurement, with the electronics configuration scheme shown in Fig. 3.3.

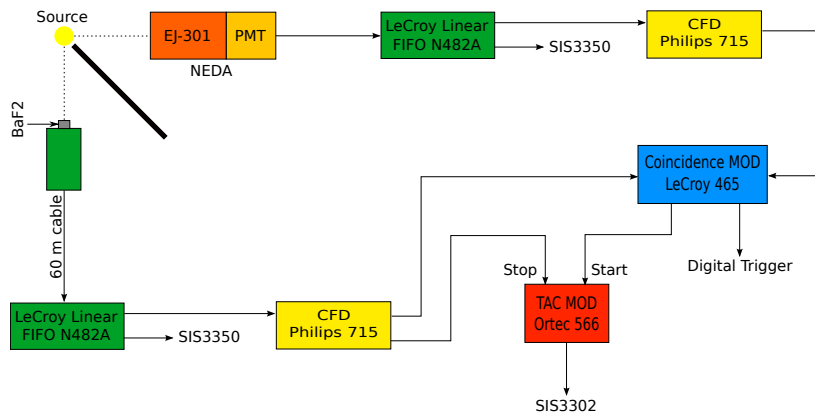


Figure 3.3: Electronics set-up used for the timing characterization of NEDA detector

The two detectors, BaF₂ and NEDA, were placed perpendicularly to each other at a distance of 50 mm and 170 mm from the ⁶⁰Co source, respectively. In order to minimize the scattering of γ rays from one detector to the other a lead shield was placed between them. The *High Voltage* (HV) for the Hamamatsu PMT was set in order to see the ⁶⁰Co *Compton Edge* (CE) at -1.70 V. The anode signals from the detectors were sent to the two channels of a LeCroy N428A linear fan-in/fan-out (FIFO) unit, using a 60 m cable for the fast BaF₂ signals. The outputs of the linear FIFO were connected to the SIS3350 sampling ADC, in order to have the digitized waveforms for digital analysis, and to an analog CFD units of type Phillips 715 to perform the analog timing, that serves also as trigger for digitizer. A LeCroy 465 module was used to select the coincidences between both detectors; this signal, time aligned with the NEDA one, was sent as start input to an Ortec 566 TAC unit, while for the stop, a delayed BaF₂ CFD signal was used. Finally the signals from the TAC module were digitized with the SIS3302.

Table 3.2: BaF₂ scintillator detector features

Density [g/cm ³]	4.88
Melting point [K]	1627
Thermal expansion coefficient [C ⁻¹]	18.410 ⁻⁶
Cleavage plane	<111>
Hardness [Mho]	3
Hygroscopic	slightly
Wavelength of emission max [nm]	310, 220(195)
Lower wavelength cutoff [nm]	135
Refractive index at emission max	1.5 (310 nm) 1.54 (220 nm)
Primary decay time [ns]	630 (slow) 0.6 - 0.8 (fast)
Light yield [photons/keV γ]	10 (slow) 1.8 (fast)
Photoelectron yield [% of NaI(Tl)] (for γ -rays)	16 (slow) 3 (fast)

An energy calibration of the digitized signals was necessary, for this reason four different γ -ray sources were used as reference. The CE of the γ -rays spectra from ²²Na, ¹³⁷Cs, ⁶⁰Co, and the photopeak for the low-energy 59.5 keV line from a ²⁴¹Am source were selected. For each source, the total charge integral spectrum was drawn (see Fig. 3.4), and then fitted in order to find the uncalibrated values associated to the corresponding CE or photopeak energies.

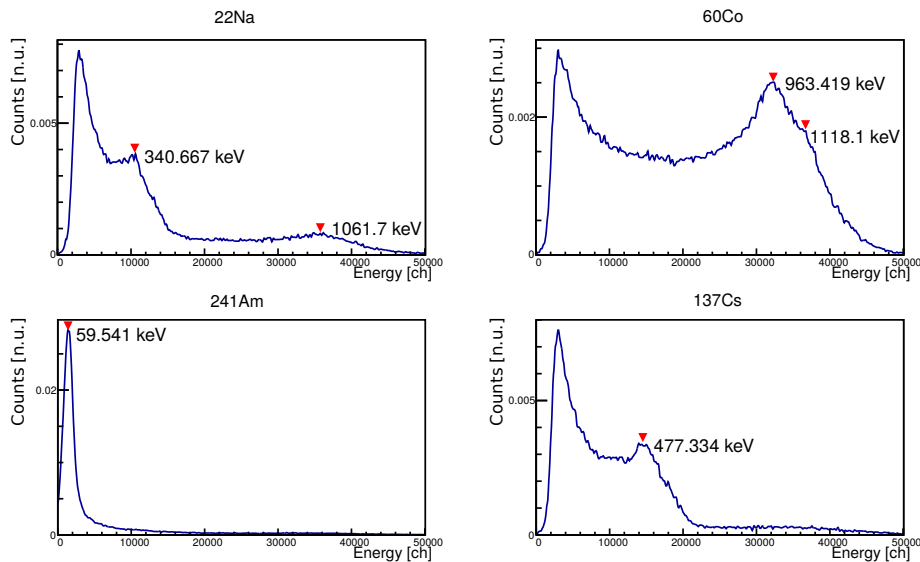


Figure 3.4: Uncalibrated energy spectrums of ²²Na, ¹³⁷Cs, ⁶⁰Co and ²⁴¹Am γ -ray sources. The red markers show their Compton Edges and photopeak, with the corresponding energies.

A calibration of the TAC unit was also performed, using as start the NEDA signals, and as stop the same delayed pulses. This process was iterated with several delays to obtain the Fig. 3.5.

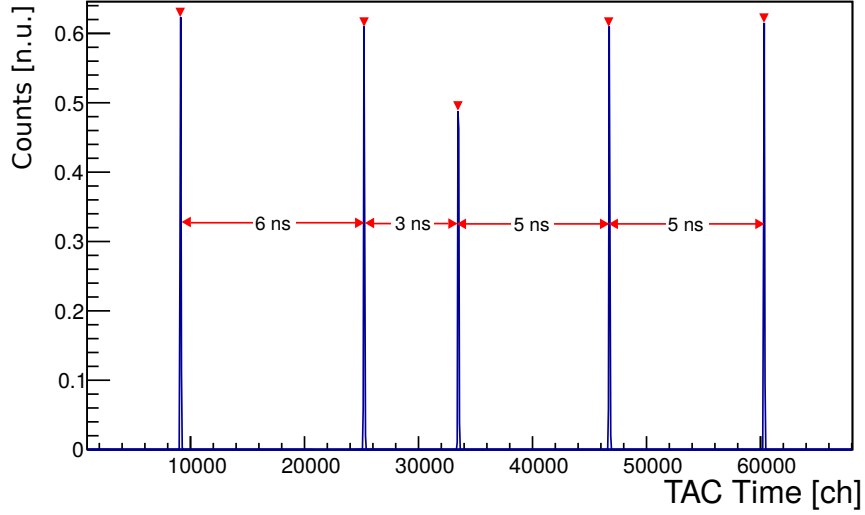


Figure 3.5: Uncalibrated TAC timing using as start the NEDA signals, and as stop the same delayed pulses.

A linear fit was then performed between the uncalibrated value and their corresponding references for both the TAC signals and energy spectrum, finding the following calibration parameters:

$$\begin{aligned} \text{Energy [keVee]} &= p_1 \text{Energy [ch]} + p_0 \\ \text{Time [ns]} &= c_1 \text{Time [ch]} \end{aligned} \quad (3.1)$$

$$\begin{aligned} p_1 &= (2.57 \pm 0.01) 10^{-2} \text{keVee/ch} \\ p_0 &= (5.6 \pm 0.3) 10^3 \text{keVee} \\ c_1 &= (3.711 \pm 0.007) 10^{-4} \text{ns/ch} \end{aligned} \quad (3.2)$$

The digital timing was then evaluated as time difference between the events of BaF₂ and NEDA. The distribution of these differences, shown in Fig. 3.6, was fitted with Eq. 2.4 to evaluate the FWHM, parameter used to evaluate the timing performance.

3.2.1 CFD Parameters Optimization

In order to obtain the best possible results from the timing algorithm, an optimization of the parameters was necessary. For each detectors, a 100 keVee energy slice around the CE was selected to avoid possible errors from time walk effects, then

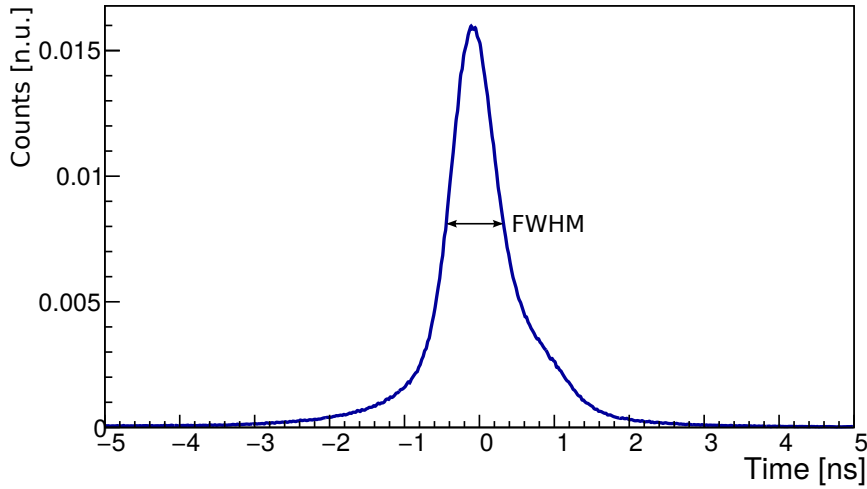


Figure 3.6: Digital timing normalized distribution of 2×10^6 events over the whole energy spectrum. The FWHM of the distribution is shown as timing performance indicator.

the digital timing was produced for several χ and δ CFD parameters configurations for both detectors. The parameters that optimize the FWHM are:

$$\begin{array}{ll}
 \mathbf{NEDA} & \chi = 0.32 \quad \delta = 10 \text{ sample} \\
 \mathbf{BaF}_2 & \chi = 0.22 \quad \delta = 3 \text{ sample}
 \end{array} \tag{3.3}$$

Using these parameters, the same procedure was followed for several ZCL values over the whole energy spectrum, in order to reduce the time walk effect. The obtained values are:

$$\begin{array}{ll}
 \mathbf{NEDA} & \text{ZCL} = 2 \text{ ch} \\
 \mathbf{BaF}_2 & \text{ZCL} = 10 \text{ ch}
 \end{array} \tag{3.4}$$

3.2.2 Results

With the calibrated values and optimized algorithms, the analysis was performed over 2×10^6 events. The digital and analog time distributions were produced for energy slice of 200 keVee, from 0 to 1200 keVee. For each one the FWHM was calculated, in order to compare the performance of the detector at different energies. Fig. 3.7 and Fig. 3.8 show these distributions for digital and analog timing respectively.

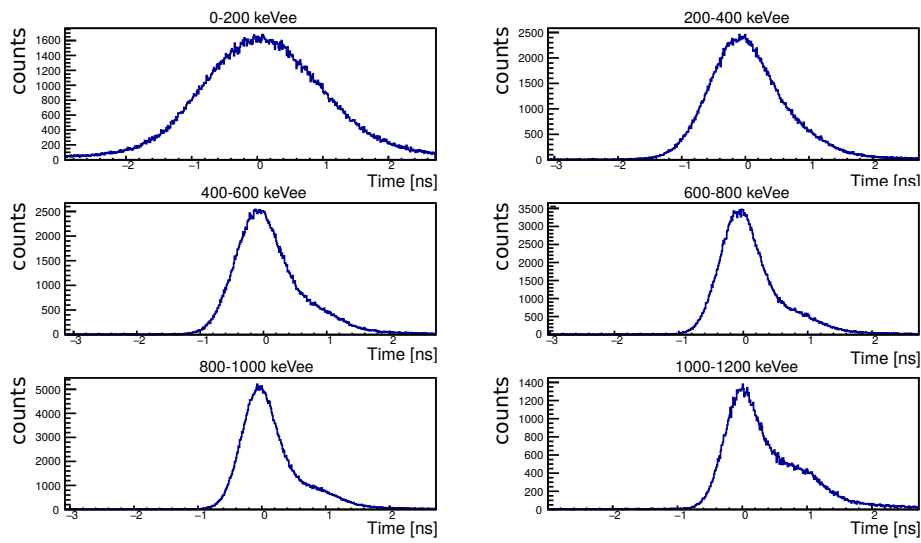


Figure 3.7: Analog timing distribution for different energy ranges of 200 keVee width. For each one the FWHM was calculated.

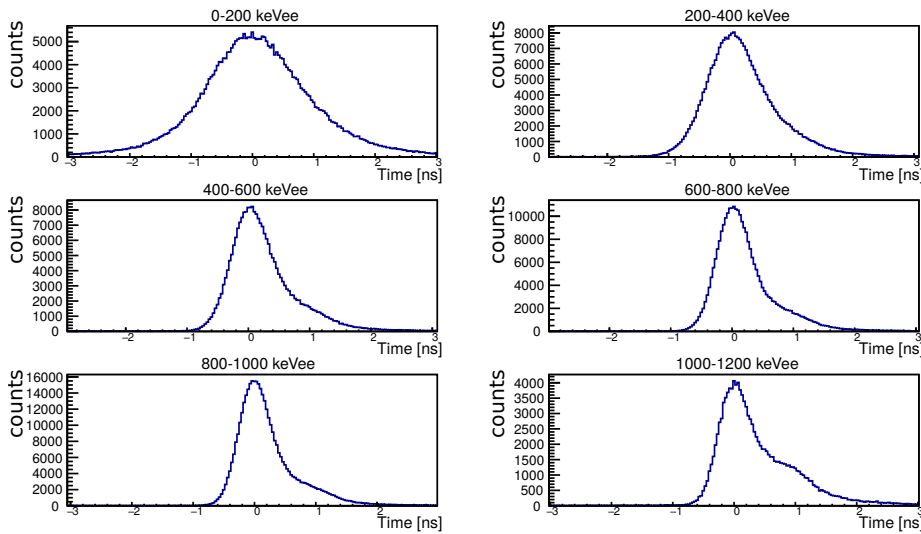


Figure 3.8: Digital timing distribution for different energy ranges of 200 keVee width. For each one the FWHM was calculated.

The digital timing distribution as function of energy is shown in Fig. 3.9. The detector reach its best performance in the range 800-1000 keVee, having a FWHM value of 636(2) ps.

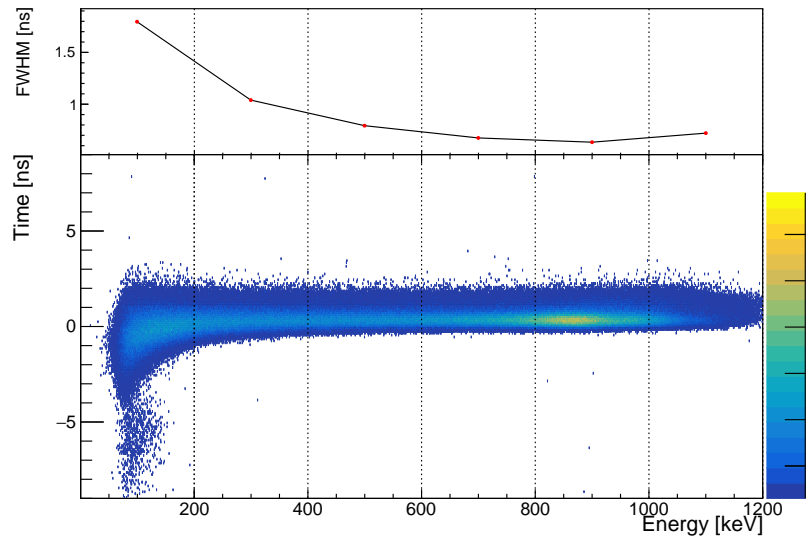


Figure 3.9: Digital timing distribution as a function of energy. The top line shows the FWHM for each corresponding energy gate.

The digital analysis performed allowed to reach better results with respect to analog electronics, as displayed by Fig. 3.10, showing the FWHM of both methods for each energy gate.

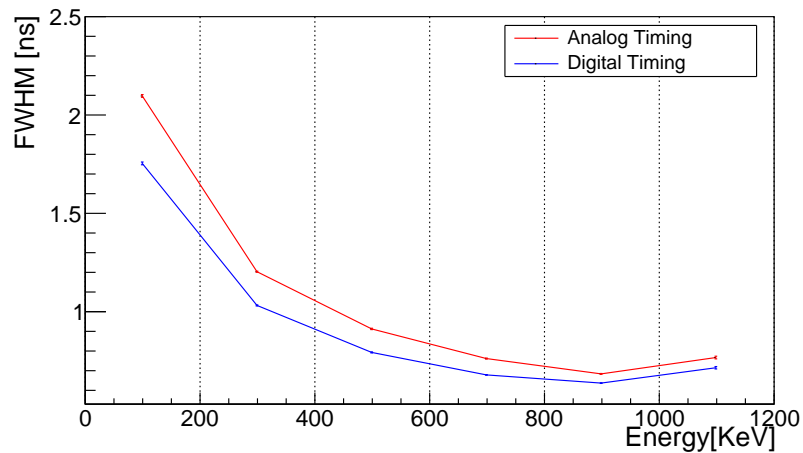


Figure 3.10: FWHM values of digital and analog methods as a function of energy.

Fig. 3.10 shows an increase of the FWHM for energy values greater than 1000 KeV. This is well understood as an effect of γ rays multi-scattering inside the scintillator, which happens for energies beyond the CE of ^{60}Co . This behaviour produces signals with a worst timing.

3.3 Neutron- γ Discrimination Measurement

In order to test the NEDA detector on NGD four methods were selected. TOF and *Zero Cross Over* (ZCO) technique were used to characterize the analog configuration, while CC and IRT methods, described in Sec. 2.2, were the digital implemented algorithms. Analog ZCO was performed using a Bartek NDE-202 module, its Z/C output gives the zero crossing time of a bipolar signal obtained reshaping the original anode waveform with means of CR-RC filters. The time differences within Z/C and CFD signals are dependent on the slow component of the pulse, reaching greater values for neutrons.

The neutron source used in the experiment was a ^{252}Cf sample, which decay mostly by alpha emission or spontaneous fission. The two detectors, NEDA and BaF_2 , were placed perpendicularly to each other at a distance of 700 mm and 50 mm from the source, respectively. In addition, as it was done for the timing measurement, a lead shield was set between the two detectors in order to minimize the scattering between them (see Fig. 3.11).

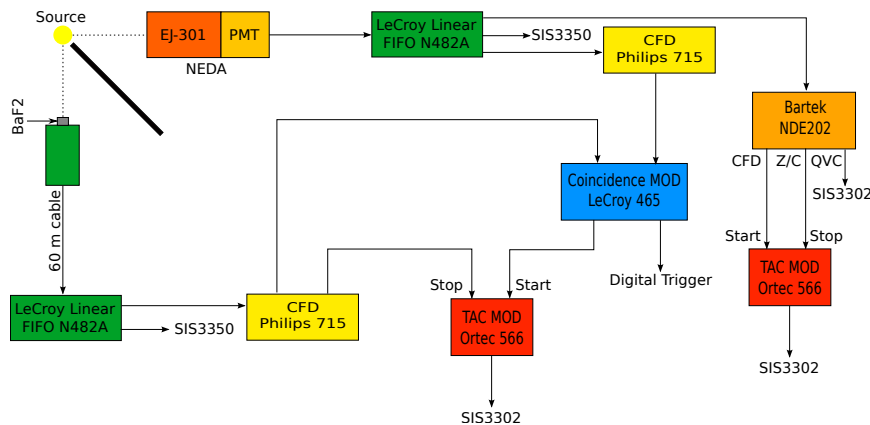


Figure 3.11: Electronics set-up used for NGD characterization of the NEDA detector

The anode signals from the detectors were sent to a Linear FIFO of model LeCroy N428A and then connected to the sampling ADC and the analog electronics, to perform both TOF and PSA analysis. After sending the two signals from the FIFO to a CFD module of type Phillips 715, an Ortec 566 TAC unit was used to obtain the TOF. It was started with the coincidences from a LeCroy 465 module, aligned with NEDA timing signals, and stopped with the delayed timing signals of the BaF_2 detector. To perform the analog ZCO, the CFD and Z/C signals from Bartek were used as start and stop, respectively, for a second Ortec 566 TAC. The QVC output from Bartek module was digitized with the SIS3302, like the signals from the two TAC modules. Having changed the experimental set-up, a new calibration was necessary. The same ^{22}Na , ^{137}Cs , ^{60}Co and ^{241}Am γ -ray sources were used to perform the energy and QVC calibration.

3.3.1 Analog NGD

The TOF distribution obtained from 2×10^6 events is displayed as a function of QVC in Fig. 3.12. The bending of the neutron shape is due to the increasing energy of the particle, bringing to smaller TOF value for higher energy neutrons.

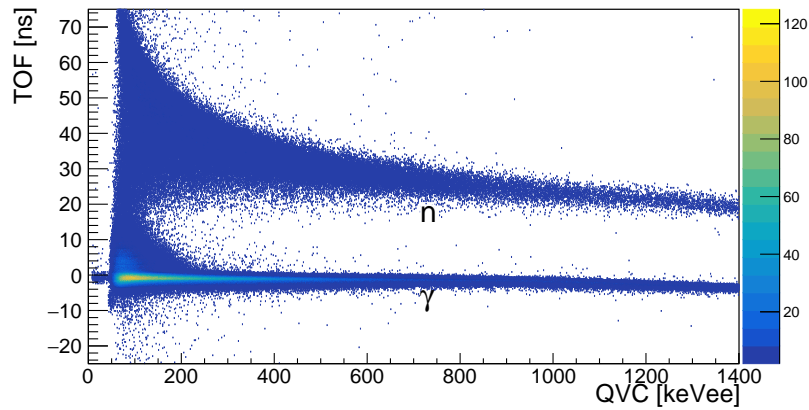


Figure 3.12: 2-D density plot of TOF vs QVC of 2×10^6 events.

Using energy slices of 100 keVee width, the study of the efficiency of the different PSA methods was performed. The FOM value was used to evaluate their performance. Fig. 3.13 shows the ZCO distribution as function of QVC. The bending of the FOM line for QVC values greater than 800-900 keVee is explained by nonlinearities of Bartek module. The two distribution of neutrons and γ rays, indeed, start to bend and get closer for high energies, resulting in a smaller FOM value.

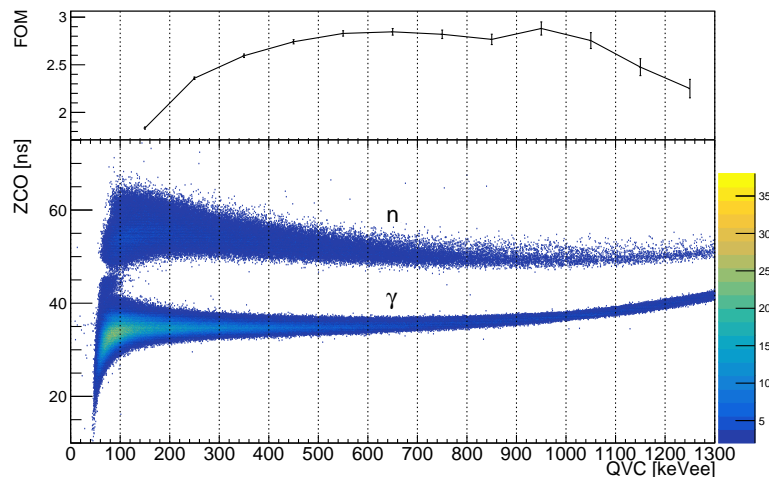


Figure 3.13: 2-D density plot of ZCO vs QVC of 2×10^6 events. The top line shows the FOM value for each corresponding energy gate.

The 2-D density plot of the ZCO vs TOF is displayed in Fig. 3.14. The figure shows two distinct cluster of events, identified as neutrons and γ rays.

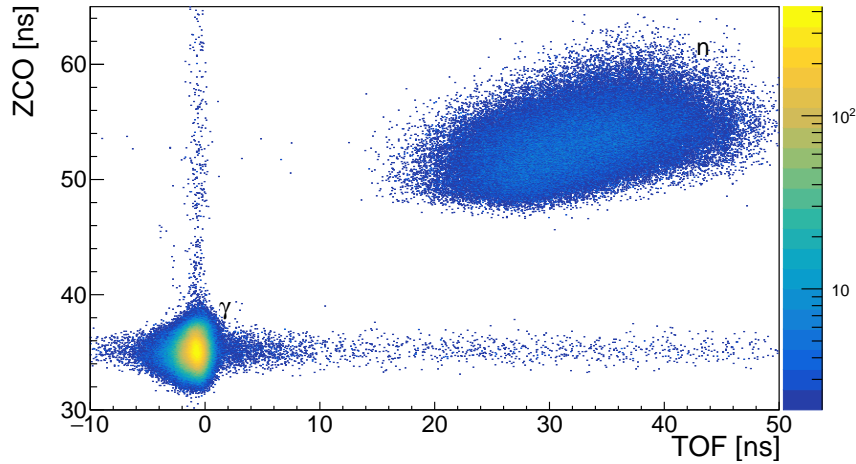


Figure 3.14: 2-D density plot of ZCO vs TOF. The two cluster represent γ rays and neutrons. The figure was obtained setting a QVC threshold of 150 keVee.

3.3.2 Digital NGD

The two digital PSA methods, CC and IRT, were used over the digitized NEDA signals. CC algorithm was set with a long integration gate ranging from 20 samples before and 180 samples after the CFD timing, while the short integration gate was started 20 samples after the timing. IRT was performed using a rise fraction of 0.91.

As done for the ZCO analysis, the FOM values of the two distributions were calculated with energy slices of 100 keVee width. Fig. 3.15 and Fig. 3.16 show the two distributions as a function of energy, displaying the FOM value for each energy gate.

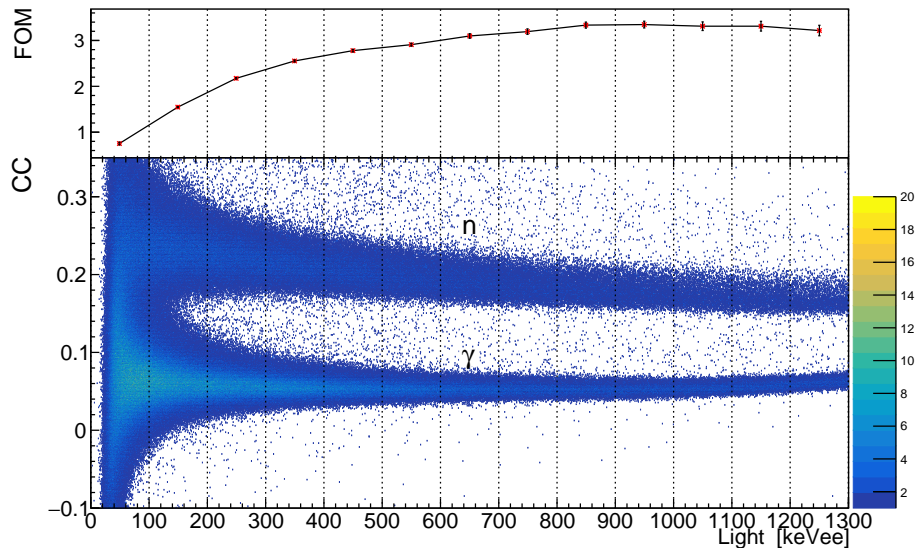


Figure 3.15: 2-D density plot of CC vs Light. The top line shows the FOM value for each energy gate.

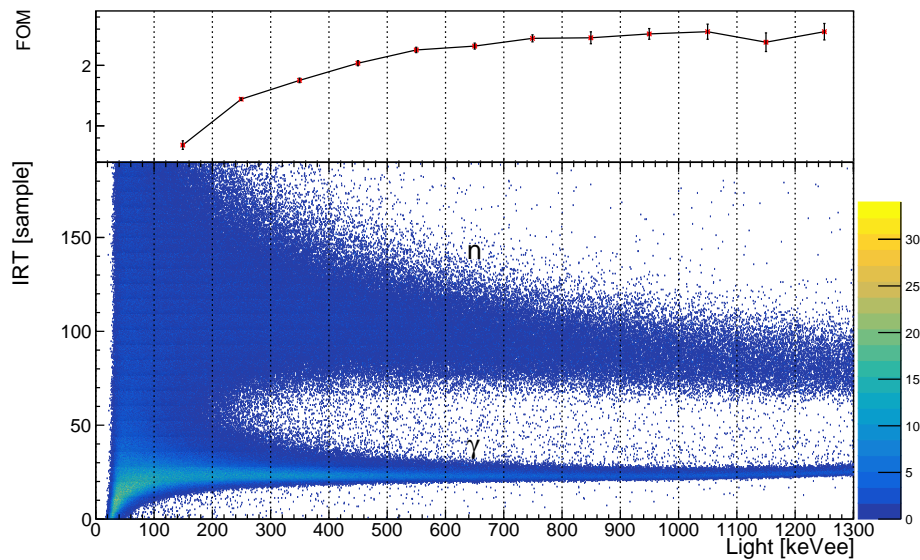


Figure 3.16: 2-D density plot of IRT vs Light. The top line shows the FOM value for each energy gate.

Finally, a 2-D density plot of the two methods was created as done for the two analog techniques. The presence of two clusters represents γ rays and neutrons and gives a rough idea of the NGD performance of the two digital techniques.

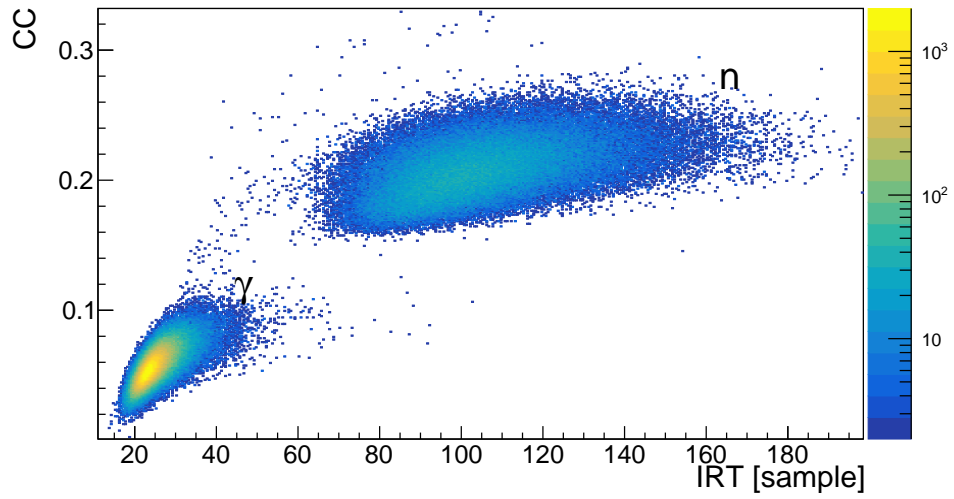


Figure 3.17: 2-D density plot of CC vs IRT, showing the two cluster representing γ ray and neutron. The figure was obtained setting a threshold of 200 keVee.

Summary and Conclusions

The characterization measurements of the definitive NEDA detector are discussed in this thesis. The detector was tested for timing and *Neutron- γ Discrimination* (NGD) performances, making use of both digital analysis techniques and analog electronics.

The timing experiment made use of a commercial 1" \times 1" BaF₂ scintillator detector (see Tab. 3.2) as reference and a ⁶⁰Co γ -ray source. The analog parts used a Philips 715 *Constant Fraction Discrimination* (CFD) module to produce the logic timing signals of the two detectors and an Ortec 566 TAC to evaluate the time difference between them. In parallel a digital CFD algorithm was developed, using a cubic spline interpolation with derivative bound continuity condition up to second order to reconstruct the digitized signals. The sampling *Analog to Digital Converter* (ADC) used in the measurements were a SIS3350 500 MHz digitizer for the anode waveforms and a SIS3302 200 MHz digitizer (see Tab. 2.1) for the TAC signals.

The results, listed in Tab. 3.3, show a better timing performance for digital analysis for all the range, with the best FWHM in the range 800-1000 keV.

Table 3.3: Analog and Digital FWHM values of timing distribution.

Energy range [keVee]	0-200	200-400	400-600	600-800	800-1000	1000-1200
Analog FWHM [ps]	2097(7)	1199(3)	910(3)	757(3)	682(2)	766(7)
Digital FWHM [ps]	1752(7)	1031(3)	790(3)	675(2)	636(2)	711(6)

The NGD measurement was performed using a ²⁵²Cf neutron source. *Time of Flight* (TOF) and *Zero Cross Over* (ZCO) techniques were selected for the analog evaluations. The TOF was obtained with a TAC module started and stopped by the CFD signals of the two detectors. The ZCO discriminator was evaluated with a Bartek NDE202 module. The time difference between the Z/C and CFD output of the device were measured with a TAC module. Digital *Pulse Shape Analysis* (PSA) was accomplished with a *Charge Comparison* (CC) and *Integrated Rise Time* (IRT) algorithms. The former uses as discriminator parameter the ratio between two integrals of the pulse, a short one for the slow component and a long one to renormalise. The latter uses instead the rising time of the *Cumulative Integra-*

tion (CI) function, which depends on the particle type. The FOM values obtained from the three NGD technique are displayed in Fig. 3.18.

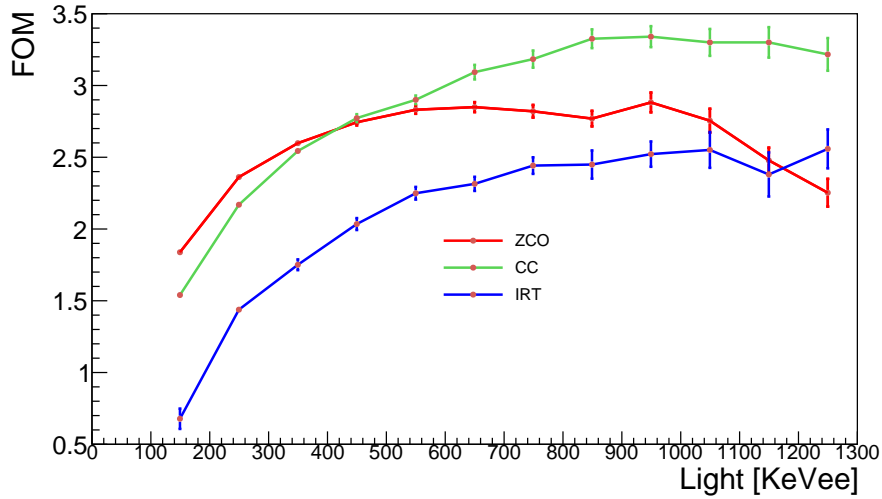


Figure 3.18: FOM values of ZCO, CC and IRT techniques as a function of light.

For light under 400 keVee the analog ZCO technique has the best NGD performance, with a FOM of ~ 2.50 . Instead, for high energy events, the CC has the best FOM. IRT has in general the lowest FOM values. This may be due to a not perfect choice of the algorithm parameters. For this reason further measurements and optimizations will be necessary. The measurements have shown excellent timing and NGD capabilities for the first NEDA detector. In its future experimental campaign NEDA will be coupled to AGATA spectrometer, this combination will allow a step forward on the study of nuclear structure far from the valley of stability.

Bibliography

- [1] Ö. Skeppstedt et al. “The EUROBALL neutron wall – design and performance tests of neutron detectors”. In: *Nuclear Instruments and Methods in Physics Research Section A: Accelerators, Spectrometers, Detectors and Associated Equipment* 421.3 (1999), pp. 531–541. ISSN: 0168-9002. DOI: [http://doi.org/10.1016/S0168-9002\(98\)01208-X](http://doi.org/10.1016/S0168-9002(98)01208-X). URL: <http://www.sciencedirect.com/science/article/pii/S016890029801208X>.
- [2] J. Ljungvall, M. Palacz, and J. Nyberg. “Monte Carlo simulations of the Neutron Wall detector system”. In: *Nuclear Instruments and Methods in Physics Research Section A: Accelerators, Spectrometers, Detectors and Associated Equipment* 528.3 (2004), pp. 741–762. ISSN: 0168-9002. DOI: <http://doi.org/10.1016/j.nima.2004.05.032>. URL: <http://www.sciencedirect.com/science/article/pii/S016890020400988X>.
- [3] D.G. Sarantites et al. ““Neutron Shell”: a high efficiency array of neutron detectors for γ -ray spectroscopic studies with Gammasphere”. In: *Nuclear Instruments and Methods in Physics Research Section A: Accelerators, Spectrometers, Detectors and Associated Equipment* 530.3 (2004), pp. 473–492. ISSN: 0168-9002. DOI: <http://doi.org/10.1016/j.nima.2004.04.243>. URL: <http://www.sciencedirect.com/science/article/pii/S0168900204010861>.
- [4] G. Jaworski et al. “Monte Carlo simulation of a single detector unit for the neutron detector array NEDA”. In: *Nuclear Instruments and Methods in Physics Research Section A: Accelerators, Spectrometers, Detectors and Associated Equipment* 673 (2012), pp. 64–72. ISSN: 0168-9002. DOI: <http://doi.org/10.1016/j.nima.2012.01.017>. URL: <http://www.sciencedirect.com/science/article/pii/S0168900212000514>.
- [5] T. Hüyük et al. “Conceptual design of the early implementation of the Neutron Detector Array (NEDA) with AGATA”. In: *Eur. Phys. J. A* 52.3 (2016), p. 55. DOI: [10.1140/epja/i2016-16055-8](https://doi.org/10.1140/epja/i2016-16055-8). URL: <https://doi.org/10.1140/epja/i2016-16055-8>.
- [6] A. Raggio et al. *Timing Characterization of the NEDA Detector*. Annual Report. INFN, Laboratori Nazionali di Legnaro Viale dell’Università, 2 I-

- 35020 Legnaro (Padova) Italy, 2016. URL: <http://www.lnl.infn.it/~annrep>.
- [7] A. Raggio et al. *Pulse Shape Analysis of the NEDA Detector*. Annual Report. INFN, Laboratori Nazionali di Legnaro Viale dell'Università, 2 I-35020 Legnaro (Padova) Italy, 2016. URL: <http://www.lnl.infn.it/~annrep>.
- [8] F. J. Egea Canet et al. “Digital Front-End Electronics for the Neutron Detector NEDA”. In: *IEEE Transactions on Nuclear Science* 62.3 (June 2015), pp. 1063–1069. ISSN: 0018-9499. DOI: 10.1109/TNS.2015.2392159.
- [9] F. J. Egea Canet et al. “A New Front-End High-Resolution Sampling Board for the New-Generation Electronics of EXOGAM2 and NEDA Detectors”. In: *IEEE Transactions on Nuclear Science* 62.3 (June 2015), pp. 1056–1062. ISSN: 0018-9499. DOI: 10.1109/TNS.2015.2433021.
- [10] S. Das. “A simple alternative to the Crystal Ball function”. In: (2016). arXiv: 1603.08591 [hep-ex].
- [11] V. Modamio et al. “Digital pulse-timing technique for the neutron detector array NEDA”. In: *Nuclear Instruments and Methods in Physics Research Section A: Accelerators, Spectrometers, Detectors and Associated Equipment* 775 (2015), pp. 71–76. ISSN: 0168-9002. DOI: <http://doi.org/10.1016/j.nima.2014.12.002>. URL: <http://www.sciencedirect.com/science/article/pii/S0168900214014430>.
- [12] X.L. Luo et al. “Test of digital neutron–gamma discrimination with four different photomultiplier tubes for the NEutron Detector Array (NEDA)”. In: *Nuclear Instruments and Methods in Physics Research Section A: Accelerators, Spectrometers, Detectors and Associated Equipment* 767 (2014), pp. 83–91. ISSN: 0168-9002. DOI: <http://doi.org/10.1016/j.nima.2014.08.023>. URL: <http://www.sciencedirect.com/science/article/pii/S0168900214009437>.
- [13] T. Hüyük et al. *Monte Carlo Simulations for the Different Configurations of the NEDA Array*. Annual Report. INFN, Laboratori Nazionali di Legnaro Viale dell'Università, 2 I-35020 Legnaro (Padova) Italy, 2011. URL: <http://www.lnl.infn.it/~annrep>.